

# Direct observation of the transverse near field of an edge excitation and associated slow secondary dynamics in a fractional quantum Hall state

Yunhyeon Jeong,<sup>1</sup> Akinori Kamiyama,<sup>1</sup> John N. Moore,<sup>1</sup> Takaaki Mano,<sup>2</sup> Ken-ichi Sasaki,<sup>3</sup> Yuuki Sugiyama,<sup>4</sup> Tokiro Numasawa,<sup>4</sup> Masahiro Hotta,<sup>1,5</sup> and Go Yusa<sup>1</sup>

<sup>1</sup>*Department of Physics, Tohoku University, Sendai 980-8578, Japan*

<sup>2</sup>*National Institute for Materials Science, Tsukuba, Ibaraki 305-0047, Japan*

<sup>3</sup>*NTT Research Center for Theoretical Quantum Information, NTT, Inc., 3-1 Morinosato Wakamiya, Atsugi, Kanagawa 243-0198, Japan*

<sup>4</sup>*Institute for Solid State Physics, The University of Tokyo, Chiba, 277-8581, Japan*

<sup>5</sup>*Leung Center for Cosmology and Particle Astrophysics, National Taiwan University, Taipei 10617, Taiwan (R.O.C.)*

(Dated: May 22, 2026)

We report stroboscopic time-resolved photoluminescence (PL) microscopy and spectroscopy revealing the transverse near field of an edge excitation in a  $\nu = 1/3$  fractional quantum Hall (FQH) state. Time-resolved  $y$ - $t$  maps reveal an immediate PL response extending more than  $30 \mu\text{m}$  into the bulk transverse to the edge when the edge magnetoplasmon (EMP) passes the mesa boundary. The nearly instantaneous nature of this long-range response identifies it as the non-radiative, quasi-electrostatic near field, revealing the EMP as a spatially extended collective excitation rather than a strictly one-dimensional charge-density oscillation. We also observe secondary bulk-side responses distinct from the immediate transverse near-field response. The coexistence of these immediate and secondary responses shows that electrically launched edge excitations produce bulk-side dynamics on widely separated time scales.

Fractional quantum Hall (FQH) states [1, 2] are a paradigmatic realization of strongly correlated topological matter, in which electron-electron interactions give rise to an incompressible bulk with fractionalized quasiparticle excitations [3, 4] and chiral edge degrees of freedom [5]. The coexistence of a gapped bulk and gapless boundary excitations makes FQH systems a natural platform for studying how a strongly correlated topological phase is reflected in its boundary physics.

Quantum Hall edge channels provide a versatile platform for coherent electronic interferometry and electron quantum optics [6–8], as well as for chiral heat transport [9, 10]. These capabilities have motivated broader directions including flying-qubit architectures [11], quantum energy teleportation [12, 13], and analog simulations of expanding-universe dynamics [14–18]. At the same time, edge dynamics in a FQH system should not be reduced to one-dimensional transport along the boundary. Rather, the edge is the boundary manifestation of an incompressible many-body state [5, 19], and an edge excitation can involve not only chiral charge propagation but also electromagnetic fields and responses of the surrounding quantum Hall fluid. Directly resolving this spatially extended structure is therefore essential for understanding edge dynamics as part of the full FQH medium.

Among dynamical edge excitations, those launched electrically in quantum Hall systems have been widely studied as edge magnetoplasmons (EMPs), collective low-frequency edge modes propagating along the boundary [20–24]. Since an edge excitation involves charge motion, it is naturally accompanied by an electromagnetic field, as is also implicit in early EMP theories [25, 26]. Experimentally, however, EMPs have usually been viewed and probed as one-dimensional charge-density waves propagating along the edge.

Here we report a long-range transverse optical response

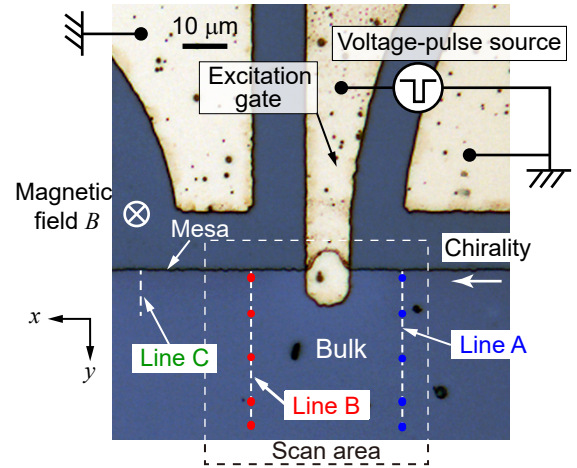


FIG. 1. Optical microscope image of the measurement device. The excitation gate was driven by a voltage-pulse source (see SM for the details). The dashed rectangle labeled “Scan area” corresponds to Fig. 3. Lines A, B, and C indicate the measurement paths for Figs. 2 and 4. Grounded electrodes are part of coplanar waveguide structures [27].

accompanying an edge excitation in the  $\nu = 1/3$  Laughlin state [2]. In the simplest idealized low-energy description, the edge of this state contains a single chiral charge mode. The response extends tens of micrometers into the bulk and remains observable more than  $40 \mu\text{m}$  downstream from the excitation gate, consistent with a response arising from the near-field component of an EMP. Time-resolved measurements further reveal secondary bulk-side responses distinct from the immediate transverse near-field response, suggesting that an edge excitation can additionally induce longer-lived bulk-side responses.

The device was fabricated from a wafer containing a 15-nm GaAs/Al<sub>0.2</sub>Ga<sub>0.8</sub>As quantum well (QW) [24], grown on a Si-doped substrate that serves as a back gate for tuning the electron density  $n$  in the QW. All measurements reported here were performed in the  $\nu = 1/3$  FQH state at  $B = 14$  T and a temperature of 40–50 mK. The excitation gate (Fig. 1) was driven by a voltage-pulse source; the source configuration and biasing details are given in the Supplemental Material (SM). In all measurements reported here, the rectangular component of the voltage pulse had a duration of approximately 2 ns. Applying a voltage pulse to the excitation gate launches an edge excitation that propagates leftward along the mesa edge.

Laser pulses generated by a mode-locked Ti:sapphire laser were synchronized to the voltage-pulse source. The laser pulse width was  $\sim 1$  ps, and the repetition period  $T_{\text{rep}}$  was either  $\sim 13$  ns or  $\sim 52$  ns when a pulse picker was used to reduce the laser repetition rate. The laser beam was focused onto the sample through an objective lens, yielding a diffraction-limited spot size of  $0.77 \mu\text{m}$ , and the emitted photoluminescence (PL) was collected by the same objective and sent to a spectrometer equipped with a CCD detector. The focal position was controlled using piezoelectric stages. Each spectrum was accumulated over  $N_{\text{rep}} = T_{\text{exp}}/T_{\text{rep}}$  repetitions, with a total exposure time of  $T_{\text{exp}} = 10\text{--}20$  s. The relative delay between the laser and voltage pulses was controlled electronically to enable stroboscopic time-resolved measurements. Throughout the manuscript,  $t$  denotes the delay time for the corresponding measurement configuration. The absolute origin of  $t$  is defined separately for each configuration, as described in the SM.

Around  $\nu = 1/3$ , the PL spectrum contains singlet and triplet trion features associated with different electron-spin configurations [28, 29]. Although the detailed line shape in the FQH regime is affected by many-body correlations and is not modeled quantitatively here, changes in the trion peak energies and amplitudes provide a sensitive local probe of the surrounding two-dimensional electron system, as established in previous optical studies of quantum Hall systems [27, 29–34].

First, to characterize the spatial dependence of the edge-excitation-induced PL response, we recorded micro-PL spectra at five transverse positions along Lines A and B, as defined in Fig. 1. The PL spectra were recorded at  $t = -3.0$  ns. Since the pulse period is  $\sim 13$  ns, this timing is equivalent to approximately 10 ns after the edge excitation reached  $y = 0$  on Line B in the preceding cycle. Along Line A, located upstream of the excitation gate, the PL spectra remain almost unchanged regardless of whether periodic voltage pulses are applied (blue lines) or not (black dotted lines), as shown in Fig. 2(a). In contrast, along Line B, located downstream of the excitation gate, the spectra differ markedly from those along Line A. Specifically, along Line B, the application of periodic voltage pulses enhances the low-energy singlet feature and suppresses the high-energy triplet feature (Fig. 2(b)). This tendency is most pronounced near the mesa boundary at  $y \approx 8 \mu\text{m}$ ; at  $y \approx 18 \mu\text{m}$  the singlet intensity still exceeds the triplet intensity, and the singlet feature remains visible even at  $28 \mu\text{m}$  from the

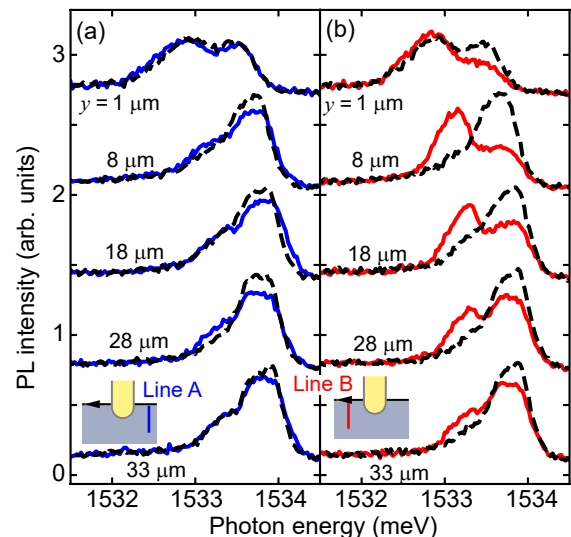


FIG. 2. (a) and (b) Micro-PL spectra measured as snapshots at positions along the  $y$  direction, perpendicular to the mesa boundary defined by  $y = 0$ :  $y = 1, 8, 18, 28,$  and  $33 \mu\text{m}$ . The delay time is  $t = -3.0$  ns for both panels (see SM for more details). (a) Spectra measured along Line A,  $16 \mu\text{m}$  upstream from the center of the excitation gate. (b) Spectra measured along Line B,  $16 \mu\text{m}$  downstream from the center of the excitation gate. The dotted curves show spectra measured without the excitation pulse. Insets in (a) and (b) schematically indicate the measurement locations (Lines A and B), as defined in Fig. 1. The pulse amplitude is  $\pm 100$  mV for both panels. The spectra shown in (b) were measured along Line B under the same voltage-pulse configuration and  $T_{\text{rep}} \sim 13$  ns condition as the time-resolved measurements presented later in Figs. 4(c) and 4(d).

mesa boundary. It is remarkable that signatures of the edge excitation remain visible even at points  $28 \mu\text{m}$  into the bulk and as late as 10 ns after the excitation reached  $y = 0$  on Line B. Since no comparable spectral change is observed upstream, this behavior is unlikely to arise from simple heating.

To confirm the spectral modification induced by the edge excitation, we performed similar micro-PL measurements over the scan area indicated by the dashed rectangle in Fig. 1, including Lines A and B. Figures 3(b)–(d) show snapshots of the triplet PL intensity measured at  $t = -3.0$  ns, corresponding to a delay of approximately 10 ns from the time when the edge excitation passed  $y = 0$  on Line B.

Without a voltage pulse applied to the excitation gate (Fig. 3(b)), the PL intensity is nearly symmetric on the upstream and downstream sides of the gate, aside from surface contaminants, which can be identified in the reflectance map (Fig. 3(a)) and fine spatial fluctuations consistent with a weak disorder-induced potential landscape [35–37]. Such disorder is commonly attributed to remote ionized donors in modulation-doped heterostructures, for example, Si donors in  $\delta$ -doping layers separated from the QW [35]. The characteristic energy scale of this disorder potential is on the order of 0.1 meV, as reported in Ref. [37].

When the voltage pulse is applied, the triplet PL intensity on the downstream side is suppressed, and the affected region

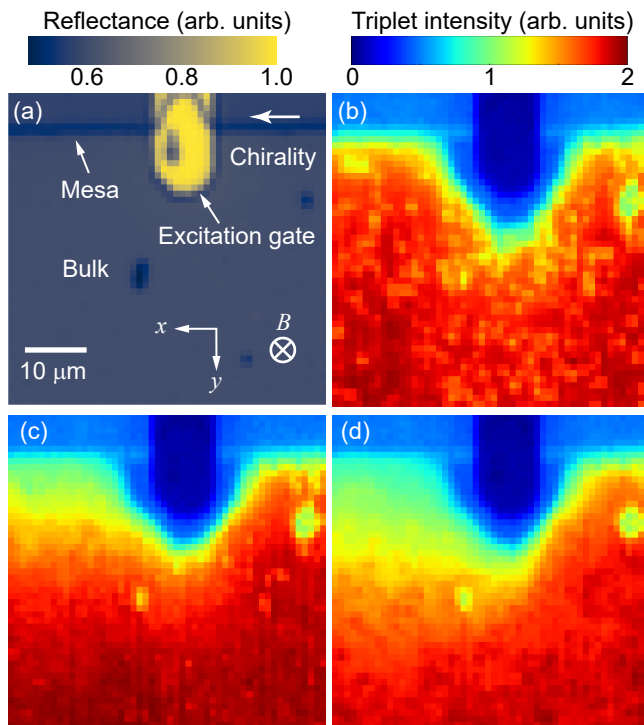


FIG. 3.  $51 \times 50 \mu\text{m}^2$  spatial maps measured in the region indicated as the scan area in Fig. 1. (a) Reflectance map acquired with the same optical setup at 40–50 mK; the yellow region indicates the excitation gate. (b)–(d) Triplet PL intensity maps of the same region measured as snapshots at  $t = -3.0$  ns with an exposure time of 10 s. Here, the triplet PL intensity was obtained by integrating the PL spectrum over 1533.45–1534.70 meV, without spectral fitting. (b) Triplet PL intensity map recorded with no voltage pulse applied to the excitation gate. (c) and (d) Maps obtained with a bipolar voltage pulse applied to the excitation gate. The pulse amplitude is  $\pm 50$  mV in panel (c) and  $\pm 100$  mV in panel (d). The dark blue region in Figs. 3(b)–3(d) corresponds to the region occluded by the excitation gate.

extends more than  $10 \mu\text{m}$  from the mesa boundary in the  $y$  direction (Figs. 3(c) and 3(d)); whereas no comparable change is observed upstream. Increasing the pulse amplitude from  $\pm 50$  mV (Fig. 3(c)) to  $\pm 100$  mV (Fig. 3(d)) enhances this downstream suppression. At the same time, the contrast associated with the random potential becomes less visible across the image, consistent with heating induced by the voltage pulse.

In this stroboscopic measurement, because the PL spectra are accumulated at  $T_{\text{rep}} \sim 13$  ns, phenomena with relaxation times longer than 13 ns cannot be captured in time. To investigate the origin of the edge-excitation-induced influence over a wide bulk region, we therefore increased  $T_{\text{rep}}$  from  $\sim 13$  ns to  $\sim 52$  ns, i.e., by a factor of four, and examined the possible contribution of longer relaxation processes to the observed decay.

The PL spectra were recorded at spatial positions scanned along the  $y$  direction on Line C, located  $42 \mu\text{m}$  downstream from the center of the excitation gate. From these spectra, the triplet peak energy shift and amplitude ratio were extracted as functions of  $t$  and  $y$ , as mapped in Figs. 4(a) and 4(b).

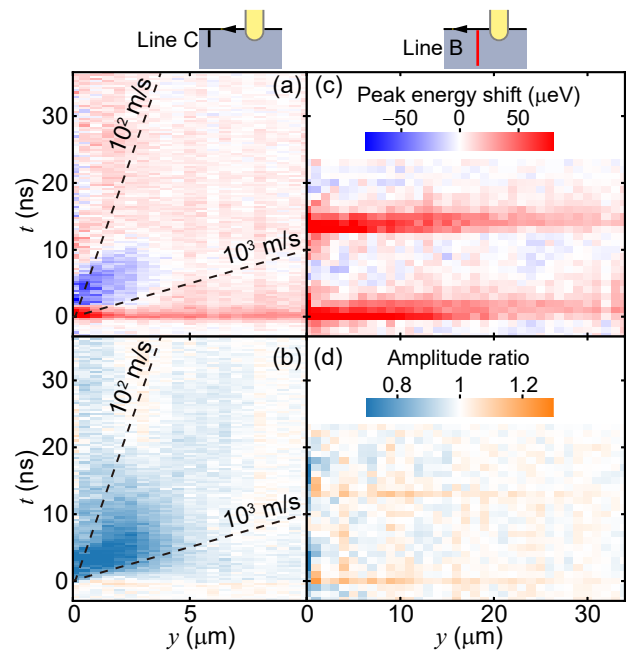


FIG. 4. Triplet PL peak-energy shift [(a), (c)] and amplitude ratio [(b), (d)], shown as color maps as functions of  $y$  and  $t$ . Panels (a) and (b) were measured along Line C,  $\sim 42 \mu\text{m}$  downstream of the excitation gate, with  $T_{\text{rep}} \sim 52$  ns; panels (c) and (d) were measured along Line B,  $16 \mu\text{m}$  downstream, with  $T_{\text{rep}} \sim 13$  ns. The absolute origin of  $t$  is defined separately for the Line-C and Line-B measurements; see the SM for details. The voltage-pulse configuration and biasing conditions are described in the SM.

The spectral fitting procedure and the definitions of the peak energy shift and amplitude ratio are described in the SM. For comparison, the same analysis was applied to data acquired along Line B, with  $T_{\text{rep}} \sim 13$  ns [Figs. 4(c) and 4(d)].

The edge excitation is clearly visible in all panels around  $t \sim 0$  ns and  $y \sim 0 \mu\text{m}$ , where the mesa boundary is located. Another notable feature is a triplet peak energy shift extending over nearly the entire  $y$  range around  $t \sim 0$ , appearing as a horizontal red line in both Figs. 4(a) and (c). In Fig. 4(c), two such horizontal lines are visible because responses from two periods are captured. Although weaker than the energy shift, a similar horizontal feature is also visible in the amplitude-ratio maps. The associated PL modulation extends more than  $30 \mu\text{m}$  into the bulk, far exceeding microscopic length scales associated with the edge charge distribution, such as the magnetic length  $l_B = \sqrt{\hbar/eB} = 6.9$  nm and the compressible-strip width  $a \sim 0.1\text{--}0.3 \mu\text{m}$  [36].

If the observed response were due to a bulk excitation propagating with a finite transverse velocity, one would expect a delay that increases with  $y$ , appearing as a slanted feature emerging from  $t = 0$  ns and  $y = 0 \mu\text{m}$  in the  $y$ - $t$  map. Instead, the triplet peak energy shift forms a horizontal feature: it appears at the same timing as the signal from the launched edge excitation near the mesa boundary and extends into the bulk without an observable transverse delay. Moreover, upstream Line A data measured in the same manner as Figs. 4(c) and

4(d) clearly show no triplet peak energy shift (Fig. S3 in the SM). This comparison supports the interpretation that the immediate bulk-side response is associated with the downstream-propagating edge excitation rather than a direct influence of the excitation gate or a spatially uniform optical or electrical artifact. We therefore identify this horizontal feature in the  $y$ - $t$  maps as the transverse near field accompanying the EMP, and not as a slower excitation.

Here, “near field” refers to the non-radiative, quasi-electrostatic component of the electromagnetic near field accompanying the EMP charge-density oscillation. According to Ref. [26], the transverse structure of an EMP with wavenumber  $k$  is governed by a Fredholm-type integral eigenvalue equation for the charge-density oscillation [their Eq. (6)], whose kernel is given by the modified Bessel function  $K_0(|k||y - y_1|)$ . Note that our  $x$  and  $y$  axes are defined oppositely to those in Ref. [26], with edge propagation along  $x$  in our case; we have relabeled their variables accordingly. The kernel behaves as  $K_0(s) \approx -\ln s + \text{const}$  for  $s \ll 1$  and decays as  $K_0(s) \propto e^{-s}/\sqrt{s}$  for  $s \gg 1$ . Thus, while the charge-density oscillation is concentrated within the boundary strip of width  $a$ , the electrostatic response associated with a long-wavelength component extends into the bulk over a characteristic transverse length scale of order  $\sim 1/|k|$ .

The characteristic EMP wavenumber  $|k|$  is set by the temporal bandwidth of the launched excitation: the excitation-gate waveform has  $\tau \sim 0.5$ – $2$  ns (set by the  $\sim 2$  ns pulse width and the  $\sim 200$  ps rise/fall times), corresponding to frequency components on the order of  $f \sim 0.5$ – $2$  GHz. Using a representative propagation speed  $v \sim 10^5$  m/s gives  $\lambda \sim v/f \sim 50$ – $200$   $\mu\text{m}$  and hence  $1/|k| = \lambda/2\pi \approx 8$ – $32$   $\mu\text{m}$ , consistent with the observed long-range modulation of the trion PL.

The EMP is a collective excitation in which charge-density oscillations are inseparably accompanied by electromagnetic fields. Nevertheless, its transverse near-field component has been explored experimentally far less than EMP propagation along the edge. This is largely because the near field is non-radiative, and conventional electrical probes predominantly access signals integrated along the propagation direction, with limited sensitivity to the spatial distribution of the field extending into the bulk [20–23]. In contrast, the trion PL response provides a local optical readout of the 2DEG environment, enabling direct visualization of the long-range transverse influence associated with the EMP near field.

Apart from the immediate transverse near-field response discussed above, a broad delayed response is visible near the mesa boundary in the 52-ns data [Figs. 4(a) and (b)]. This response evolves over several tens of nanoseconds and extends gradually into the bulk. Although this response is broad and lacks a sharp propagating front, its fastest visible spatial evolution corresponds to an apparent rate no greater than  $\sim 10^3$  m/s, substantially slower than the primary bulk magnetoplasmon velocity reported for gate-induced bulk excitations in Ref. [27].

The broad delayed response is clearly visible when  $T_{\text{rep}} \sim 52$  ns [Figs. 4(a) and (b)], whereas it is not clearly resolved

when  $T_{\text{rep}} \sim 13$  ns [Figs. 4(c) and (d)]. This difference is consistent with the slow time scale of the broad delayed response. For the 13-ns repetition period, the broad delayed response may not fully relax before the next voltage pulse arrives. Under periodic excitation, such incomplete relaxation can produce a cycle-averaged modification of the PL spectrum, rather than a well-resolved time-dependent feature within a single delay window.

We also note a weak residual response on the positive-delay side of the immediate near-field response at  $t \approx 0$ . Unlike the broad delayed response, which is mainly visible near the mesa boundary, this residual response remains visible even far into the bulk, where the immediate near-field response is observed. This spatial behavior suggests that the residual response is associated with the near-field response rather than with the broad delayed response. Since this residual response may reflect either local relaxation following the near-field response or the finite temporal profile of the near-field response itself, we do not assign it to a separate dynamical mode.

Neither the broad delayed response nor the residual response can be attributed to trion recombination. The singlet and triplet trion PL decay times are on the order of a few hundred picoseconds [38], much shorter than the time window shown in Fig. 4.

In light of the above, the PL spectra measured along Line B at  $t = -3.0$  ns in Fig. 2(b) should be interpreted as a cycle-averaged spectral modification, rather than as a snapshot of only the immediate transverse near-field response. This interpretation is supported by the PL spectra shown in Fig. S2 of the SM. In the Line-B data measured with  $T_{\text{rep}} \sim 13$  ns, the spectra at  $t = 10.0$  ns still show a pronounced voltage-pulse-induced modification relative to the spectra measured without the voltage pulse: the singlet feature remains enhanced and the triplet feature remains suppressed [Fig. S2(a)]. In contrast, in the Line-C data measured with  $T_{\text{rep}} \sim 52$  ns, the spectra at  $t = 9.9$  ns show a much weaker triplet suppression, as indicated by the recovered high-energy triplet feature [Fig. S2(b)]. This comparison supports the interpretation that, under the 13-ns repetition condition, the triplet suppression does not fully relax before the next voltage pulse arrives. The residual spectral modification can therefore accumulate over repeated cycles, producing a cycle-averaged spectrum that varies only weakly within the available delay window. This explains why the relaxation of the triplet suppression is not resolved in Figs. 4(c) and 4(d), and why the triplet suppression observed in Figs. 2(b) and 3 reflects accumulated contributions from delayed and residual responses rather than the immediate near-field response alone.

In summary, we investigated electrically launched edge excitations and their accompanying bulk-side responses using space- and time-resolved microscopic PL spectroscopy. Our measurements provide direct experimental evidence that an EMP in the  $\nu = 1/3$  FQH state produces an immediate transverse response extending more than  $30$   $\mu\text{m}$  into the bulk, far beyond  $l_B$ . The absence of an observable transverse propagation delay identifies this response as the non-radiative, quasi-

electrostatic near-field component accompanying the EMP. In addition, we observed a broad delayed response and a weak residual response following the near-field response, indicating that the edge excitation also produces responses in the surrounding FQH fluid. These results extend the experimental picture of quantum Hall edge dynamics from one-dimensional charge-density propagation along the boundary to a spatially extended charge-and-field excitation that also perturbs the adjacent bulk region. More broadly, they provide a concrete example showing that a dynamical edge mode in a topological electronic system can be characterized not only by its propagation along the boundary, but also by the accompanying electromagnetic field and the bulk-side response it induces.

The authors thank T. Takayanagi for fruitful discussions. This work was supported by a Grant-in-Aid for Scientific Research (Grant Nos. 21H05182, 21H05188, and 24H00399) from the Ministry of Education, Culture, Sports, Science, and Technology (MEXT), Japan. T.N. was supported by MEXT KAKENHI Grant Nos. 23K13094 and 24H00944 and by JST PRESTO Grant No. JPMJPR2359. We are grateful to the YITP workshop YITP-T-25-01 held at YITP, Kyoto University, where part of this work was carried out.

- 
- [1] D. C. Tsui, H. L. Stormer, and A. C. Gossard, *Phys. Rev. Lett.* **48**, 1559 (1982).
- [2] R. B. Laughlin, *Phys. Rev. Lett.* **50**, 1395 (1983).
- [3] R. De-Picciotto, M. Reznikov, M. Heiblum, V. Umansky, G. Bunin, and D. Mahalu, *Nature* **389**, 162 (1997).
- [4] L. Saminadayar, D. Glatli, Y. Jin, and B. c.-m. Etienne, *Physical Review Letters* **79**, 2526 (1997).
- [5] X.-G. Wen, *Rev. of Mod. Phys.* **89**, 041004 (2017).
- [6] Y. Ji, Y. Chung, D. Sprinzak, M. Heiblum, D. Mahalu, and H. Shtrikman, *Nature* **422**, 415 (2003).
- [7] G. Fève, A. Mahe, J.-M. Berroir, T. Kontos, B. Placais, D. Glatli, A. Cavanna, B. Etienne, and Y. Jin, *Science* **316**, 1169 (2007).
- [8] E. Bocquillon, V. Freulon, J.-M. Berroir, P. Degiovanni, B. Plaçais, A. Cavanna, Y. Jin, and G. Fève, *Science* **339**, 1054 (2013).
- [9] G. Granger, J. Eisenstein, and J. Reno, *Physical review letters* **102**, 086803 (2009).
- [10] M. Banerjee, M. Heiblum, A. Rosenblatt, Y. Oreg, D. E. Feldman, A. Stern, and V. Umansky, *Nature* **545**, 75 (2017).
- [11] A. Assouline, L. Pugliese, H. Chakraborti, S. Lee, L. Bernabeu, M. Jo, K. Watanabe, T. Taniguchi, D. Glatli, N. Kumada, *et al.*, *Science* **382**, 1260 (2023).
- [12] G. Yusa, W. Izumida, and M. Hotta, *Phys. Rev. A* **84**, 032336 (2011).
- [13] M. Hotta, J. Matsumoto, and G. Yusa, *Phys. Rev. A* **89**, 012311 (2014).
- [14] M. Hotta, Y. Nambu, Y. Sugiyama, K. Yamamoto, and G. Yusa, *Phys. Rev. D* **105**, 105009 (2022).
- [15] S. S. Hegde, V. Subramanian, B. Bradlyn, and S. Vishveshwara, *Phys. Rev. Lett.* **123**, 156802 (2019).
- [16] Y. Nambu and M. Hotta, *Phys. Rev. D* **107**, 085002 (2023).
- [17] R. Yoshimoto and Y. Nambu, *Physics Lett. A* **529**, 130100 (2025).
- [18] Y. Sugiyama and T. Numasawa, *arXiv preprint arXiv:2506.20338* (2025).
- [19] X.-G. Wen, *Adv. Phys.* **44**, 405 (1995).
- [20] R. C. Ashoori, H. L. Stormer, L. N. Pfeiffer, K. W. Baldwin, and K. West, *Phys. Rev. B* **45**, 3894 (1992).
- [21] G. Ernst, R. J. Haug, J. Kuhl, K. von Klitzing, and K. Eberl, *Phys. Rev. Lett.* **77**, 4245 (1996).
- [22] H. Kamata, T. Ota, K. Muraki, and T. Fujisawa, *Phys. Rev. B* **81**, 085329 (2010).
- [23] M. Hashisaka, N. Hiyama, T. Akiho, K. Muraki, and T. Fujisawa, *Nature Phys.* **13**, 559 (2017).
- [24] A. Kamiyama, M. Matsuura, J. N. Moore, T. Mano, N. Shibata, and G. Yusa, *Phys. Rev. Res.* **4**, L012040 (2022).
- [25] V. Volkov and S. Mikhailov, *Zh. Eksp. Teor. Fiz.* **67** (1988).
- [26] I. L. Aleiner and L. I. Glazman, *Phys. Rev. Lett.* **72**, 2935 (1994).
- [27] Q. France, Y. Jeong, A. Kamiyama, T. Mano, K.-i. Sasaki, M. Hotta, and G. Yusa, *Phys. Rev. Lett.* **135**, 066203 (2025).
- [28] A. Wójs, J. J. Quinn, and P. Hawrylak, *Phys. Rev. B* **62**, 4630 (2000).
- [29] G. Yusa, H. Shtrikman, and I. Bar-Joseph, *Phys. Rev. Lett.* **87**, 216402 (2001).
- [30] C. Schüller, K.-B. Broocks, P. Schröter, C. Heyn, D. Heitmann, M. Bichler, W. Wegscheider, T. Chakraborty, and V. Apalkov, *Phys. Rev. Lett.* **91**, 116403 (2003).
- [31] J. N. Moore, J. Hayakawa, T. Mano, T. Noda, and G. Yusa, *Phys. Rev. Lett.* **118**, 076802 (2017).
- [32] A. Popert, Y. Shimazaki, M. Kroner, K. Watanabe, T. Taniguchi, A. Imamoğlu, and T. Smolenski, *Nano Lett.* **22**, 7363 (2022).
- [33] J. Cai, E. Anderson, C. Wang, X. Zhang, X. Liu, W. Holtzmann, Y. Zhang, F. Fan, T. Taniguchi, K. Watanabe, *et al.*, *Nature* **622**, 63 (2023).
- [34] E. Anderson, J. Cai, A. P. Reddy, H. Park, W. Holtzmann, K. Davis, T. Taniguchi, K. Watanabe, T. Smolenski, A. Imamoğlu, *et al.*, *Trion sensing of a zero-field composite Fermi liquid*, *Nature* **635**, 590 (2024).
- [35] G. Eytan, Y. Yaron, M. Rappaport, H. Shtrikman, and I. Bar-Joseph, *Phys. Rev. Lett.* **81**, 1666 (1998).
- [36] S. Ilani, J. Martin, E. Teitelbaum, J. Smet, D. Mahalu, V. Umansky, and A. Yacoby, *Nature* **427**, 328 (2004).
- [37] J. Hayakawa, K. Muraki, and G. Yusa, *Nature Nano.* **8**, 31 (2013).
- [38] A. Kamiyama, M. Matsuura, J. N. Moore, T. Mano, N. Shibata, and G. Yusa, *Appl. Phys. Lett.* **122**, 202103 (2023).

# Supplemental Material for

## Direct observation of the transverse near field of an edge excitation and associated slow secondary dynamics in a fractional quantum Hall state

Yunhyeon Jeong, Akinori Kamiyama, John N. Moore, Takaaki Mano, Ken-ichi Sasaki,  
Yuuki Sugiyama, Tokiro Numasawa, Masahiro Hotta, Go Yusa

### 1 Voltage-Pulse Source and Biasing Conditions

Voltage pulses were applied to the excitation gate to launch edge excitations propagating along the mesa boundary. Two voltage-pulse source configurations were used in this work, depending on the measurement condition. In both configurations, the applied waveform contained a rectangular voltage-pulse component with a duration of approximately 2 ns.

In the first configuration, a rectangular voltage pulse was generated by a pulse generator and fed directly to the coaxial line connected to the excitation gate, without using a bias tee. This configuration was used for the measurements shown in Figs. 2, 3, 4(c), and 4(d) of the manuscript, the Line-B spectra in Fig. S2(a) and Fig. S3. The pulse amplitude was set to  $\pm 50$  or  $\pm 100$  mV, as indicated in the corresponding figure. For the time-resolved measurements performed with this configuration, the repetition period was approximately  $T_{\text{rep}} = 13$  ns. The delay time coordinate used for these data is denoted by  $t_1$ .

In the second configuration, a negative-polarity rectangular voltage pulse was generated using an arbitrary waveform generator (AWG). The AWG output was switched from +100 mV to -100 mV for approximately 2 ns and was combined with a -0.1 V dc bias using a bias tee before being applied to the excitation gate. This configuration was used for the measurements shown in Figs. 4(a) and 4(b) of the manuscript and the Line-C spectra in Fig. S2(b). For these measurements, a pulse picker was used to reduce the repetition rate of the optical pulses, extending the repetition period by a factor of four from approximately  $T_{\text{rep}} = 13$  ns to  $T_{\text{rep}} = 52$  ns. The electrical pulse train was synchronized to this repetition period. The delay time coordinate used for these data is denoted by  $t_2$ .

These two configurations are specified here to define the experimental conditions for each data set. In the manuscript, we discuss the relative temporal evolution within each delay time coordinate, rather than directly comparing the absolute delay time offsets between data sets acquired with different circuit configurations.

### 2 Definition of Delay Time Origins

As described in Sec. 1, two voltage-pulse source configurations were used in this work. Accordingly, we used two delay time coordinates,  $t_1$  and  $t_2$ , with independently defined origins  $t_{1,0}$  and  $t_{2,0}$ . The delay time is defined as the relative time delay between the optical pulse from the Ti:sapphire laser and the voltage pulse applied to the excitation gate. Since the measurement is performed in a stroboscopic manner, the delay time is a periodic coordinate determined by the repetition of the optical and electrical excitations. Therefore, the absolute origin of the delay time coordinate is arbitrary and does not have an independent physical meaning.

The coordinate  $t_1$  is used for the data in Fig. 2, Fig. 3, Fig. 4(c), and Fig. 4(d), whereas  $t_2$  is used for the data in Fig. 4(a) and Fig. 4(b). Because these two coordinates have different origins, their absolute time offsets should not be directly compared. However, the relative time evolution within each coordinate is meaningful. Each coordinate should therefore be regarded as an operational time coordinate defined within the corresponding measurement condition.

We defined the origins  $t_{1,0}$  and  $t_{2,0}$  using the temporal response of the singlet PL amplitude  $A_{X_s^-}$  at the sample edge. For each data set, the origin was chosen as the delay time at which the temporal gradient of  $A_{X_s^-}$  becomes most negative. This convention corresponds to the steepest falling point of the PL response induced by the edge excitation and provides a consistent reference time within each delay time coordinate.

For  $t_1$ , the origin  $t_{1,0}$  was determined from the edge excitation measurement at the sample edge ( $y = 0 \mu\text{m}$ ) on Line B (Fig. 1 of the manuscript), as shown in Fig. S1(a). For this measurement, a rectangular voltage pulse with  $\pm 50 \text{ mV}$  amplitude and a pulse width of  $2 \text{ ns}$  was generated by a pulse generator and applied to the excitation gate. The gray dashed line indicates the defined origin  $t_{1,0} = 0 \text{ ns}$ .

For  $t_2$ , the origin  $t_{2,0}$  was determined in the same manner from the PL response at the sample edge on Line C (Fig. 1 of the manuscript), as shown in Fig. S1(b). For this measurement, a negative-polarity rectangular voltage pulse was generated by switching the AWG output from  $+100 \text{ mV}$  to  $-100 \text{ mV}$  for  $2 \text{ ns}$  with a repetition period of approximately  $52 \text{ ns}$ . The pulse train was offset with a  $-0.1 \text{ V}$  dc bias using a bias tee and applied to the excitation gate. The gray dashed line indicates the defined origin  $t_{2,0} = 0 \text{ ns}$ .

In the following sections, unless otherwise noted, the delay coordinate for each measurement configuration is denoted simply by  $t$ .

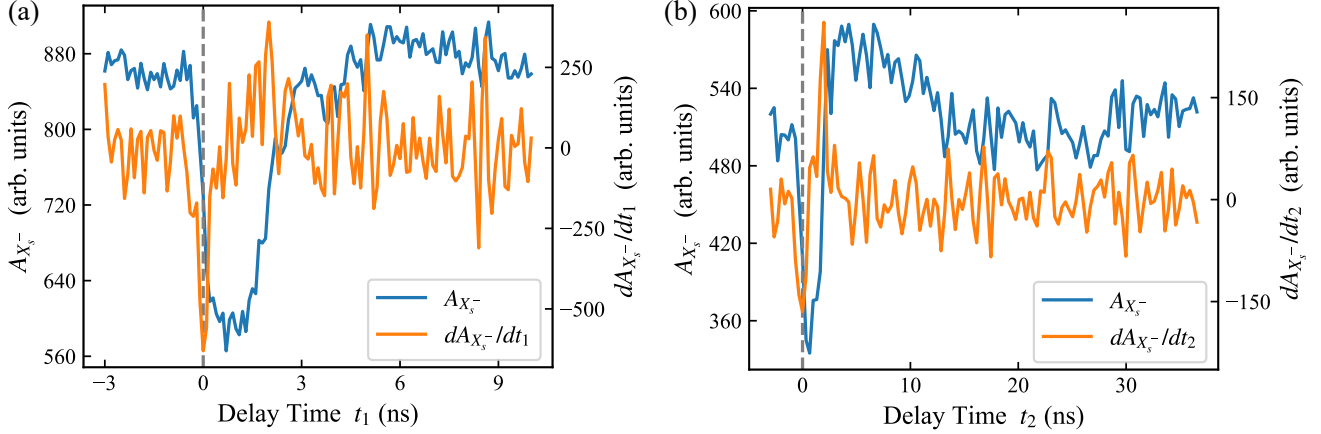


FIG. S1. Definition of the time origins used in the delay time coordinates. (a) Time evolution of the singlet PL amplitude  $A_{X_s^-}$  measured at the sample edge on Line B. The orange curve shows the temporal gradient  $dA_{X_s^-}/dt_1$ , and the gray dashed line indicates the defined time origin  $t_{1,0}$ . (b) Time evolution of  $A_{X_s^-}$  measured at the sample edge on Line C. The orange curve shows the temporal gradient  $dA_{X_s^-}/dt_2$ , and the gray dashed line indicates the defined time origin  $t_{2,0}$ .

### 3 PL Spectrum Fitting

The collected photoluminescence (PL) was sent to a spectrometer equipped with a CCD detector. The CCD output was recorded as a function of delay time  $t$  between the laser and voltage pulses, position  $(x, y)$ , and photon energy  $E$ . We denote the measured PL spectrum as  $N(t, x, y, E)$ .

For each fixed delay time and position, the PL spectrum as a function of  $E$  was fitted by the sum of two Lorentzian functions and a constant background:

$$f(E) = \frac{A_{X_s^-} \gamma^2}{(E - E_{X_s^-})^2 + \gamma^2} + \frac{A_{X_t^-} \gamma^2}{(E - E_{X_t^-})^2 + \gamma^2} + C. \quad (1)$$

Here,  $X_s^-$  and  $X_t^-$  denote the singlet and triplet trion PL peaks, respectively. The parameters  $E_{X_s^-}$  and  $E_{X_t^-}$  are the peak energies, and  $A_{X_s^-}$  and  $A_{X_t^-}$  are the peak amplitudes. Because of the normalization used in Eq. (1),  $A_{X_s^-}$  and  $A_{X_t^-}$  correspond to the peak heights, not to the integrated PL intensities. The parameter  $2\gamma$  is the full width at half maximum (FWHM), and  $C$  represents a constant background of the CCD output.

The linewidth parameter  $\gamma$  was taken to be common to the singlet and triplet components in each fit. This common linewidth was introduced to stabilize the fitting procedure by reducing the number of independent fitting parameters. This treatment is also reasonable for the present analysis because the observed linewidth is mainly limited by the spectral resolution of the spectrometer and CCD detector, and we do not discuss possible differences in the intrinsic linewidths of the singlet and triplet peaks.

The peak energies and amplitudes extracted from Eq. (1) were used to construct the PL energy shift and amplitude ratio maps shown in the manuscript. For each delay time coordinate  $t_i$  ( $i = 1, 2$ ) and each measurement position, the reference values were defined using the first three measured delay points. These three points were always located in the pre-excitation region  $t_i < 0$ .

The peak energy shift was calculated as the deviation from the reference peak energy. For the triplet peak, this is written as

$$\Delta E_{X_t^-}(t_i, x, y) = E_{X_t^-}(t_i, x, y) - \overline{E}_{X_t^-}^{\text{ref}}(x, y), \quad (2)$$

where  $\overline{E}_{X_t^-}^{\text{ref}}(x, y)$  is the average of  $E_{X_t^-}$  over the first three measured delay points at the same position.

The amplitude ratio was calculated by normalizing the fitted peak amplitude by the corresponding reference amplitude. For the triplet peak, this is written as

$$\tilde{A}_{X_t^-}(t_i, x, y) = \frac{A_{X_t^-}(t_i, x, y)}{\overline{A}_{X_t^-}^{\text{ref}}(x, y)}, \quad (3)$$

where  $\overline{A}_{X_t^-}^{\text{ref}}(x, y)$  is the average of  $A_{X_t^-}$  over the first three measured delay points at the same position. The time-resolved maps in Fig. 4 of the manuscript show the triplet peak energy shift  $\Delta E_{X_t^-}$  and the triplet amplitude ratio  $\tilde{A}_{X_t^-}$ .

## 4 Comparison of PL Spectra at Positive Delay along Lines B and C

To examine whether the triplet suppression observed in the Line-B spectra is resolved within the 13-ns repetition window, we compare PL spectra extracted from the Line-B and Line-C time-resolved data sets at a positive delay of approximately 10 ns. Figure S2 shows representative spectra at  $y = 1, 3, 5,$  and  $10 \mu\text{m}$ . The red curves were extracted from the Line-B data set used for Figs. 4(c) and 4(d) of the manuscript at  $t = 10.0$  ns, for which  $T_{\text{rep}} \sim 13$  ns. The green curves were extracted from the Line-C data set used for Figs. 4(a) and 4(b) of the manuscript at  $t = 9.9$  ns, for which  $T_{\text{rep}} \sim 52$  ns. The black dashed curves in Fig. S2(a) show spectra measured without applying the voltage pulse.

In Fig. S2(a), the Line-B spectra at  $t = 10.0$  ns still show a pronounced voltage-pulse-induced modification relative to the no-pulse spectra: the singlet feature is enhanced and the triplet feature is suppressed. In contrast, the Line-C spectra in Fig. S2(b) at  $t = 9.9$  ns show a much weaker triplet suppression, as seen from the recovered triplet feature on the higher-energy side. This contrast supports the interpretation that, in the Line-B measurement with  $T_{\text{rep}} \sim 13$  ns, the spectral modification induced by one voltage pulse does not fully relax before the next pulse arrives. Under periodic excitation, the residual spectral modification can therefore accumulate over repeated cycles and appear as a cycle-averaged spectral modification that varies only weakly within the available delay window. This accumulation makes it difficult to resolve the relaxation of the triplet suppression within the 13-ns delay window.

This comparison also indicates that the triplet suppression observed in the Line-B spectra in Fig. 2(b) of the manuscript, as well as in the triplet-intensity maps in Fig. 3, should not be interpreted as a snapshot of only the immediate transverse near-field response. Rather, these data include accumulated contributions from delayed and residual responses induced by the periodically driven edge excitation.

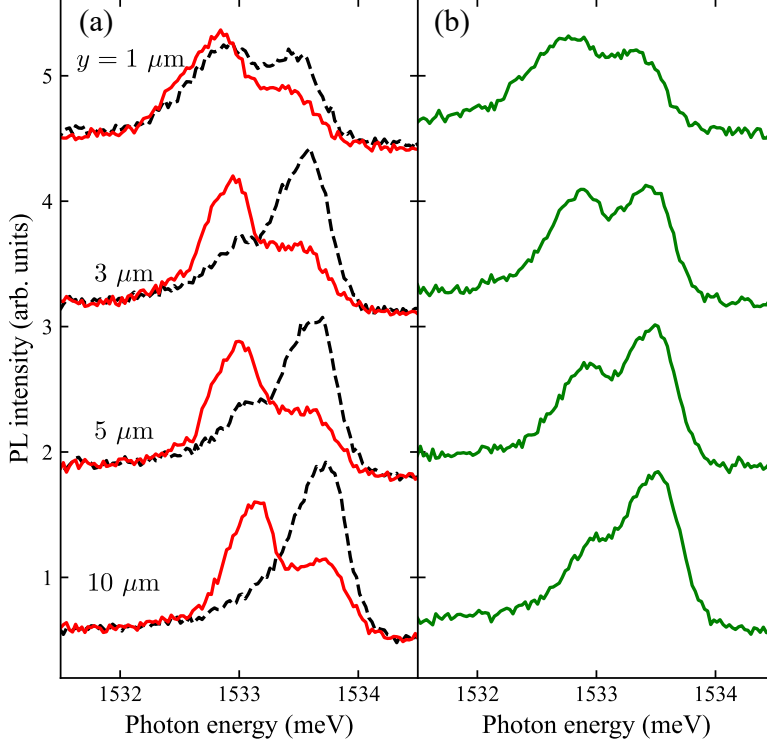


FIG. S2. Comparison of PL spectra at positive delay along Lines B and C. (a) PL spectra extracted from the Line-B time-resolved data set used for Figs. 4(c) and 4(d) of the manuscript at  $t = 10.0$  ns, measured with  $T_{\text{rep}} \sim 13$  ns. Red solid curves show spectra measured with the voltage pulse, and black dashed curves show spectra measured without applying the voltage pulse. (b) PL spectra extracted from the Line-C time-resolved data set used for Figs. 4(a) and 4(b) of the manuscript at  $t = 9.9$  ns, measured with  $T_{\text{rep}} \sim 52$  ns. Green solid curves show spectra measured with the voltage pulse. In both panels, spectra are shown at  $y = 1, 3, 5,$  and  $10 \mu\text{m}$  from top to bottom and are vertically offset for clarity.

## 5 Upstream Measurement along Line A

For comparison with the downstream Line B measurement shown in Figs. 4(c) and 4(d) of the manuscript, we performed time-resolved PL measurements along Line A. Line A is located upstream of the excitation gate, as defined in Fig. 1 of the manuscript. For this measurement, the same voltage pulse waveform was applied to the excitation gate as in Figs. 4(c) and 4(d) of the manuscript.

The obtained PL spectra were fitted and analyzed using the same fitting, reference, and normalization procedures as those used for Fig. 4. From this analysis, we extracted the triplet peak energy shift  $\Delta E_{X_t^-}$  and the triplet amplitude ratio  $\tilde{A}_{X_t^-}$ .

Fig. S3 shows the resulting maps as functions of  $y$  and  $t$  measured along Line A. The color scales are set to the same ranges as those in Fig. 4 of the manuscript. In contrast to the downstream Line B data in Figs. 4(c) and 4(d), no clear time-dependent modulation associated with the edge excitation is observed along Line A. This comparison supports the interpretation that the response observed downstream is not a spatially uniform optical or electrical artifact, but is associated with downstream propagation of the edge excitation from the excitation gate.

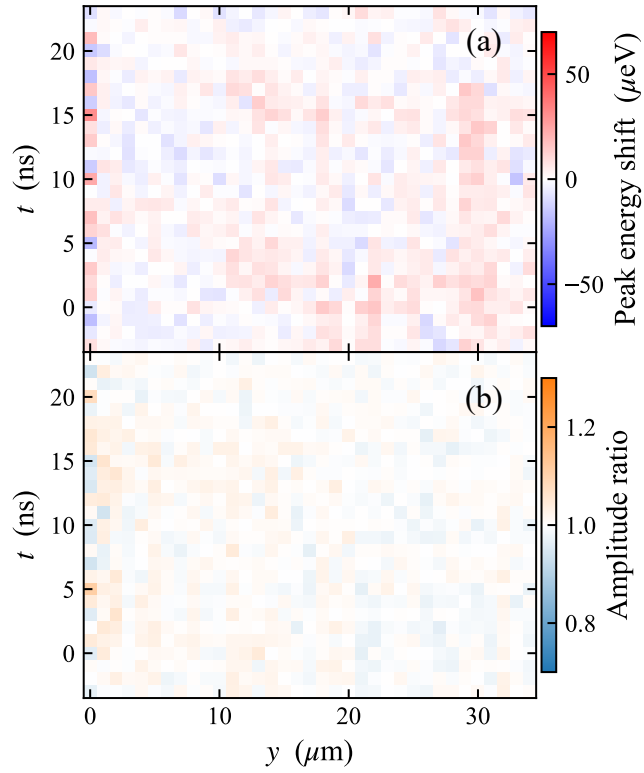


FIG. S3. Upstream PL response measured along Line A for comparison with the downstream Line B data in Figs. 4(c) and 4(d) of the manuscript. (a) Triplet peak energy shift  $\Delta E_{X_t^-}$ . (b) Triplet amplitude ratio  $\tilde{A}_{X_t^-}$ . The data were analyzed using the same fitting, reference, and normalization procedures as those used for Fig. 4, and the color scales are set to the same ranges as in Fig. 4.